**Discover** Mechanical Engineering

Research

# RVE determination and developement of an anisotropic elastic model for auxetic sheet metal

**Arash Gordanshekan**[1] · **Wolfgang Ripplinger**[1] · **Stefan Diebels**[1]

Received: 19 December 2023 / Accepted: 15 May 2024
Published online: 26 May 2024


**Abstract**
This article deals with the development of an elastic tetragonal model for the 2D auxetic rotating units structures in the framework of orthogonal transformations. The existing anisotropy in the structure was first determined by numerical simulations on the samples with different pattern orientation angles. A suitable representative volume element (RVE), which correctly represents the mechanical properties of the whole structure both in macroscale and in microscale, was then proposed by implementation of the kinematic periodic boundary conditions. In the next step, with the help of the orthogonal transformations relations, an anisotropic elastic model was developed, which correctly reflects the present tetragonal symmetry in the structure. Finally, the model parameters were identified and validated with the help of the corresponding experiments

**Keywords** Auxetics · Finite element modeling · Anisotropic elasticity · Constitutive model · Tetragonal symmetry · Computational homogenization · Periodic boundary conditions

## 1 Introduction

Generally, a microstructure can be designed in several manner to achieve different mechanical behaviors at the macroscale and that's the concept embodied by the term metamaterials. Over the past few decades, there has been significant research into metamaterials, especially concerning bioinspired and 3D-printed architectural designs, along with their characterization and modeling [1–5]. Auxetic materials or "negative Poisson's ratio materials" abbreviated as NPR materials belong to the category of metamaterials, exhibit an unusual property in which they expand laterally when stretched, instead of contracting like most materials [6, 7]. This phenomenon is the opposite of conventional material behavior, and can be observed at both the macroscopic and molecular level. However, artificial auxetic structures or so-called man-made auxetics are found much more frequently than natural ones, often as cellular materials such as honeycombs and foams [8, 9]. The unique mechanical properties of auxetic materials like negative Poisson's ratio, high energy absorption, high indentation resistance and large fracture toughness with relatively reduced density make them useful in a wide range of applications, such as medical implants, vibration dampers and protective gear [10–14].

As shown in Fig. 1 and based on the deformation mechanism, auxetic structures can be divided into the main groups of "rotating units", "chiral" and "re-entrant" structures, where the rotation, rolling up and unfolding of the structure leads to the negative Poisson's ratio respectively [11, 15–19]. A detailed study about the deformation mechanism of 2D auxetic rotating units structures can be found in our last article [20]. It has been experimentally shown by thermomechanical

✉ Arash Gordanshekan, arash.gordanshekan@uni-saarland.de | [1]Chair of Applied Mechanics, Saarland University, Campus A4 2, 66123 Saarbrücken, Germany.

analysis that the squares between the perforations undergo rigid body rotation under load. They only transfer the deformation energy through the whole metal sheet without being deformed. The direction of rotation of the squares causes the sheet to expand under uniaxial tension, which is called the auxetic effect.

Representative volume element (RVE) is an important concept in the field of computational mechanics. It is a volume of material large enough to contain statistically significant amounts of material features at the microscale, yet small enough to be computationally inexpensive to properly represent the material's behavior at a macroscale [21]. Different boundary conditions can then be applied on a RVE to determine the effective material properties of the entire system. The concept of RVE was first introduced by Hill [22] and it is currently widely used for homogenization of heterogeneous microstructures such as composite and porous materials. The shape and size of the RVE depend basically on the randomness of the geometry or microstructure, which has been extensively discussed in the framework of homogenization-based multiscale modelling [23–27]. For mechanical metamaterials such as auxetics, which are regularly composed of periodic unit cells, it is simpler to obtain an appropriate RVE than for materials with arbitrary microstructure. For such materials, the RVE typically consists of one or more unit cells, the number of which is to be determined by comparison with the fully resolved sample. The finite element (FE) analysis is one of the most common methods to deal with these systems. In order for the RVE to be a proper representative for the corresponding infinite system, the boundary effects must be eliminated somehow. This can be achieved by implementing Periodic Boundary Conditions (PBCs). Kinematic periodic boundary conditions are a set of boundary conditions applied often in a FE program, where all opposite pairs of nodes are kinematically coupled with each other, so that they deform in an identical manner and accordingly the boundary effects disappear completely [28–30]. Periodic boundary conditions are actually linear couplings between the pairs of nodes, which are supposed to be adjusted based on the given load scenario. In strain-controlled simulations, these linear equations must result in the relative motion of all pairs of nodes being equal to the specified displacement in the loading direction. This can be formulated in general for a single node pair as equation (1), where $A$ denotes the node number, $i = (1, 2, 3)$ is degree of freedom and $a$ is the constant coefficient that define the relative motion of nodes and $\hat{u}$ is a prescribed displacement value [31].

$$a_1 u_i^{A_1} + a_2 u_i^{A_2} = \hat{u}_i \tag{1}$$

Illustrated in Fig. 2 is a schematic representation of the expected structure of couplings and the corresponding linear equations among node pairs.

Anisotropy is an important common feature of many heterogeneous structures, describing their properties that differ according to the direction in which they are measured. However, by using the topology optimization methods, auxetic structures can also be designed in such a way to exhibit isotropic properties [32]. Anisotropic elasticity has been a widely investigated topic over the last decades especially due to its application to composite materials. With the exception of the complete anisotropy (triclinic system) the anisotropic elasticity is always restricted by symmetry conditions caused by material structure [33, 34]. These symmetry conditions result either from special microstructures such as composite materials or, on a macroscale, from a special geometry of the structure such as auxetic materials. All solids can be characterized in different material groups based on the number of existing symmetry planes in the structure, from triclinic materials without any symmetry plane to isotropic materials with infinite symmetry planes. With the help of Tab. 1 and Fig. 3 all possible material groups can be well represented in terms of the number of symmetry planes, where the vectors $OP$ and $OQ$ represent the normal vectors of the corresponding symmetry planes.

To understand how the symmetry properties affect the elastic behavior of an anisotropic material, we necessarily need to consider the orthogonal transformation relationships that describe the rotation about an axis or reflection about a plane mathematically. This approach leads to a reduction of the number of independent elastic constants in the fourth order elastic tensor depending on the number of symmetry planes present in the structure [35]. Although significant scientific work has been already

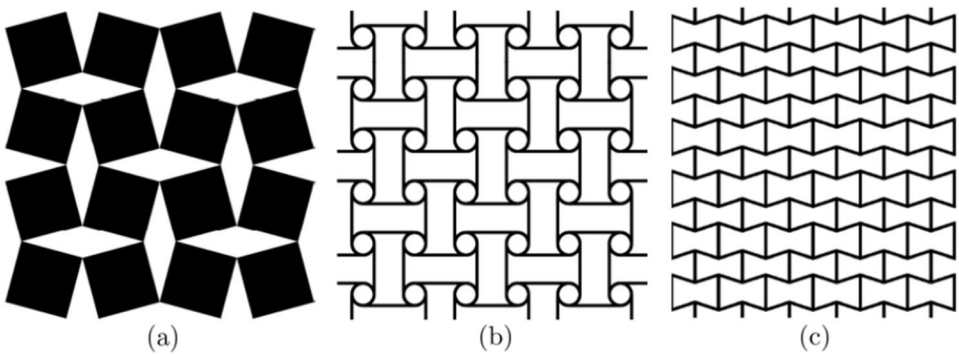


**Fig. 1** Typical auxetic structures; **a** rotating units; **b** chiral; **c** re-entrant structures

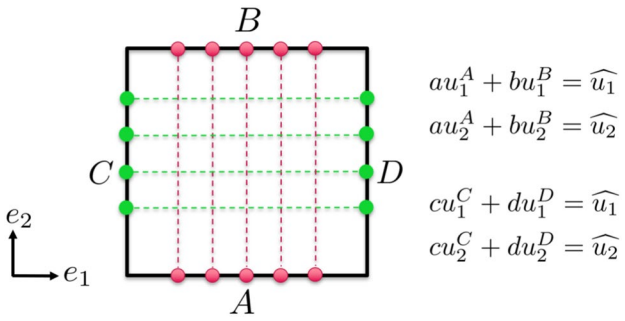


**Fig. 2** Schematic representation of the coupling between node pairs in order to implement PBCs within RVE and associated linear equations for the node pairs *AB* and *CD* in 2D

done on the elastic behavior of orthotropic and transverse isotropic materials, there is a distinct deficiency in the other types of material symmetries, which are less common and the main goal of this article is the investigation of the tetragonal symmetry of auxetic rotating units structures and the resulting elastic properties.

An orthogonal tensor represents a rigid transformation in the sense that it does not distort the shape of a body, i.e., it represents a rotary mirror or orientation of objects. Orthogonal tensors have many useful properties, such as the fact that their inverse is equal to their transpose, which makes them particularly easy to work with [36]. Let's consider two orthonormal bases $B = \{\boldsymbol{e}_1, \boldsymbol{e}_2, \boldsymbol{e}_3\}$ and $B' = \{\boldsymbol{e}'_1, \boldsymbol{e}'_2, \boldsymbol{e}'_3\}$ with an angle $\theta$ between them related by the orthogonal tensor $\boldsymbol{\Omega}$. Depending on the type of objects to be transformed according to the new base $B'$, the following relationships apply:

$$\mathbf{e}' = \boldsymbol{\Omega} \cdot \mathbf{e} \tag{2}$$

$$\mathbf{L}' = \boldsymbol{\Omega} \cdot \mathbf{L} \cdot \boldsymbol{\Omega}^{\mathrm{T}} \tag{3}$$

where $\mathbf{e}$ and $\mathbf{L}$ denote a first order tensor (vector) and a second order tensor respectively [35]. Existence of a plane of symmetry in the structure means that the objects are mirrored over this symmetry plane without changing their properties. In this case the orthogonal tensor $\boldsymbol{\Omega}$ should be able to satisfy the following expressions, namely:

$$\boldsymbol{\Omega} \cdot \mathbf{n} = -\mathbf{n} \tag{4}$$

$$\boldsymbol{\Omega} \cdot \mathbf{m} = \mathbf{m} \tag{5}$$

**Table 1** The groups of material symmetry in framework of linear anisotropic elasticity

| Type of symmetry | Number of symmetry planes | Position of normal vectors |
|---|---|---|
| Triclinic | 0 | - |
| Monoclinic | 1 | $\theta = 0$ or $\pi/2$ or $\varphi = \pi/2$ |
| Orthotropic | 3 | $\theta = 0, \pi/2$ and $\varphi = \pi/2$ |
| Trigonal | 3 | $\theta = 0$ and $\pm\pi/3$ |
| Tetragonal | 5 | $\theta = 0, \pm\pi/4, \pi/2$ and $\varphi = \pi/2$ |
| Hexagonal | 7 | $\theta = 0, \pm\pi/6, \pm\pi/3, \pi/2$ and $\varphi = \pi/2$ |
| Cubic | 9 | $\theta = 0, \pm\pi/8, \pm\pi/6, \pm\pi/4, \pi/2$ and $\varphi = \pi/2$ |
| Transverse isotropic | $\infty$ | $x_3$ axis of symmetry |
| Isotropic | $\infty$ | $\infty$ |

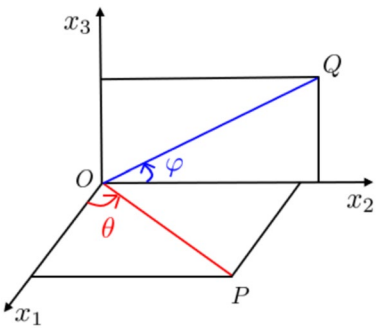


**Fig. 3** *O* represents the material origin and the vectors *OP* and *OQ* are the normals to planes of reflection symmetry mentioned in Table 1

where **n** refers to the unit vector normal to the reflection plane and **m** to the any vector on the reflection plane. The conditions 5 and 6 lead to this expression for tensor $\mathbf{\Omega}$, thus:

$$\mathbf{\Omega} = \mathbf{I} - 2\mathbf{n} \otimes \mathbf{n}^{\mathrm{T}} \tag{6}$$

where **I** denotes the second order identity tensor. In general, the vector **n** in plane can be written as:

$$\mathbf{n}^{\mathrm{T}} \hat{=} [cos\theta, sin\theta, 0] \tag{7}$$

which leads to a concrete definition of the tensor $\mathbf{\Omega}$ using Eq. 6:

$$\mathbf{\Omega}(\theta) \hat{=} \begin{bmatrix} -cos2\theta & -sin2\theta & 0 \\ -sin2\theta & cos2\theta & 0 \\ 0 & 0 & 1 \end{bmatrix} \tag{8}$$

Hooke's law is a foundational principle used to describe the elastic behaviour of materials under small strains subjected to external forces, which can be written in general case as:

$$\sigma = \overset{4}{\mathrm{C}} : \varepsilon \tag{9}$$

$$\varepsilon = S^4 \; : \; \sigma \tag{10}$$

where $\sigma$ and $\epsilon$ refer to the engineering stress and strain and **C** and **S** refer to the fourth order elastic and compliance tensor respectively. The superscript 4 denotes the order of the tensor concerned or in other words the number of bases that characterize the tensor.

As indicated in Table 1, orthotropic materials as the more occurring type of anisotropy possess three planes of symmetry at $\theta = 0, \pi/2$ und $\varphi = \pi/2$. This implies that the elasticity tensor **C** should remain invariant when subjected to the respective reflection transformations in terms of these planes of symmetry. In contracted notation, the corresponding orthogonal transformation for a fourth-order tensor such as elastic tensor **C**, which is sometimes also referred to a six-dimensional transformation, appears as follows:

$$\overset{4\prime}{\mathrm{C}} = (\Omega \otimes \Omega)^{\overset{23}{\mathrm{T}}} \; : \; \overset{4}{\mathrm{C}} \; : \; \left(\Omega^{\mathrm{T}} \otimes \Omega^{\mathrm{T}}\right)^{\overset{23}{\mathrm{T}}} \tag{11}$$

where $\overset{23}{\mathrm{T}}$ denotes a special transpose in which the second and third bases are swapped. The use of the three angles mentioned above for orthotropy in the transformation tensor $\mathbf{\Omega}$ and then applying in equation 11 and also the fact $\mathbf{C}' = \mathbf{C}$ lead to the constraints in the elasticity tensor **C** in such a way, that some components must be zero. In Voigt notation it leads to:

$$\mathbf{C}_{triclinic} = \begin{bmatrix} C_{11} & C_{12} & C_{13} & C_{14} & C_{15} & C_{16} \\ C_{21} & C_{22} & C_{23} & C_{24} & C_{25} & C_{26} \\ C_{31} & C_{32} & C_{33} & C_{34} & C_{35} & C_{36} \\ C_{41} & C_{42} & C_{43} & C_{44} & C_{45} & C_{46} \\ C_{51} & C_{52} & C_{53} & C_{54} & C_{55} & C_{56} \\ C_{61} & C_{62} & C_{63} & C_{64} & C_{65} & C_{66} \end{bmatrix}$$

$$\mathbf{C}_{orthotropic} = \begin{bmatrix} C_{11} & C_{12} & C_{13} & 0 & 0 & 0 \\ C_{21} & C_{22} & C_{23} & 0 & 0 & 0 \\ C_{31} & C_{32} & C_{33} & 0 & 0 & 0 \\ 0 & 0 & 0 & C_{44} & 0 & 0 \\ 0 & 0 & 0 & 0 & C_{55} & 0 \\ 0 & 0 & 0 & 0 & 0 & C_{66} \end{bmatrix}$$

This approach can also be employed to characterize all other elastic tensors with respect to the type of symmetry that exists in the materials. To calculate the elastic deformation, the compliance tensor **S** is preferably used instead of the

elastic tensor (Eq. 9). Finally the so-called engineering constants as the components of the tensor **S** can be calculated in Voigt's notation as a function of coefficients $S_{ij}$, which leads to:

$$\left.\begin{array}{ll} S_{ii} = \frac{1}{E_i}, & i = 1,2,3 \\ S_{kk} = \frac{1}{2G_{ij}}, & i \neq j = 1,2,3, \quad k = 4,5,6 \\ S_{ij} = \frac{-\nu_{ij}}{E_i}, & i \neq j = 1,2,3 \end{array}\right\} \Longrightarrow \mathbf{S}_{orthotropic} = \begin{bmatrix} \frac{1}{E_1} & \frac{-\nu_{21}}{E_2} & \frac{-\nu_{31}}{E_3} & 0 & 0 & 0 \\ \frac{-\nu_{21}}{E_2} & \frac{1}{E_2} & \frac{-\nu_{32}}{E_3} & 0 & 0 & 0 \\ \frac{-\nu_{31}}{E_3} & \frac{-\nu_{32}}{E_3} & \frac{1}{E_3} & 0 & 0 & 0 \\ 0 & 0 & 0 & \frac{1}{G_{13}} & 0 & 0 \\ 0 & 0 & 0 & 0 & \frac{1}{G_{23}} & 0 \\ 0 & 0 & 0 & 0 & 0 & \frac{1}{G_{12}} \end{bmatrix}$$

As can be seen from the tensor **S**, there are a total of 9 independent elastic constants describing the elastic behavior of an orthotropic material, where $E_i$, $G_{ij}$ and $\nu_{ij}$ correspond to the Young's modulus, shear modulus and Poisson's ratio's in terms of different directions.

Although the focus of this work is on elastic behavior of the auxetic structures, all stress–strain plots also include the plastic regime as additional information that is not considered in the modeling approach so far.

## 2 Material and methods

The auxetic sample to be examined is shown in Fig. 4. It made of aluminium alloy (AlMg3) with a regular pattern of rectangular perforations, which are perpendicular to each other. The perforations are cut out using a micro water jet cutter, which is available at the chair of Applied Mechanics (AM) at Saarland University. The machine provides absolute precision as well as the possibility of using the entire range of abrasive nozzles from 0.2 - 1.0 mm in micro-cutting scale. The sheet metal consists of a cellular core area and two small bulk areas at the two ends with five holes for clamping the specimen in the testing machine.

The mechanical behavior of such auxetic structures are mainly characterized by two parameters, namely volume fraction of perforations or so-called porosity ($V_p$) as well as aspect ratios of the perforations ($AR$). To calculate the porosity, only a single unit cell needs to be considered due to the periodicity. the porosity can be determined as:

$$V_p = 4\frac{A_p}{A_{uc}} = \frac{4ab}{(a+b+2c)^2} \tag{12}$$

where $a$ is the length, $b$ the width and $c$ the distance of the perforations. $A_p$ and $A_{uc}$ represent area of a single perforation and area of the unit cell respectively. The auxetic sheet metal used in this study has the parameters $a = 5\,\text{mm}$, $b = 1\text{mm}$, $c = 1\text{mm}$ and thickness of 1 mm, which results an aspect ratio of $AR = \frac{a}{b} = 5$ and a porosity of $V_p = 31\,\%$ according to Eq. 12.

### 2.1 Numerical anisotropy investigations

All simulations in this study were carried out by the commercial FE software ABAQUS® (Dassault Systems). To evaluate the anisotropy in the structure, the sheets were drawn with different pattern orientation angles from 0 ° to 90 ° in steps of 5 ° and simulated under the uniaxial tensile loading.

The element type CPS4R (4-node bilinear plane stress quadrilateral, reduced integration) with a seed size of 0.5 mm is used. The Young's modulus of 60.04 GPa and Poisson's ratio of 0.33 were applied as input parameters for the simulation, which were determined by the experiment on the bulk AlMg3. Strain-controlled tensile tests were performed, where a total displacement of 9 mm was specified, which corresponds to approx. 10% global strain for all specimens. As boundary conditions, a displacement of $U2 = 4.5\,\text{mm}$ is applied to both ends of the specimen in clamping holes so that the center of the specimen remains stationary during the deformation. The other degrees of freedom, i.e. the displacement in the $e_1$-direction and the rotation around the $e_3$-axis, are fixed, as illustrated in Fig. 5.

On the microscale, as shown in Fig. 6 the von Mises stress within the squares has low values, which according to the PEEQ-results (equivalent plastic strain) is still below the yield point of the aluminum and confirms the rigid body

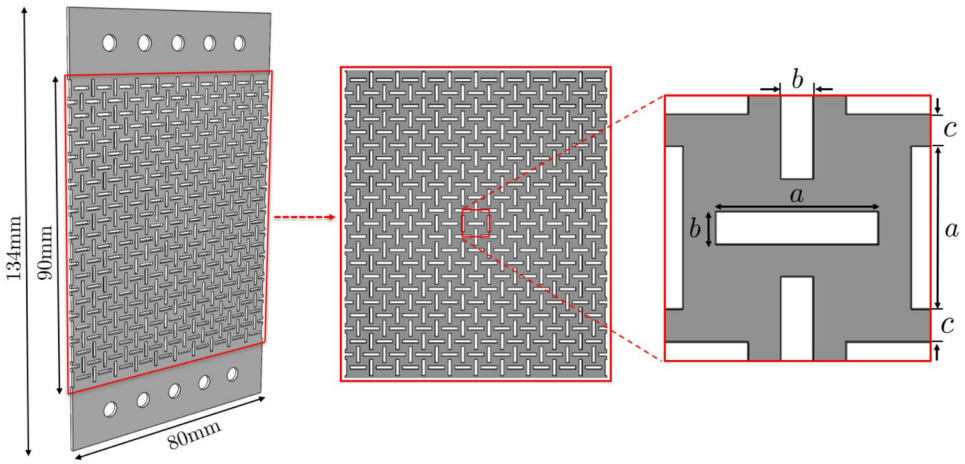


**Fig. 4** Auxetic sheet sample with rectangular perforations. From left to right: full sample including clamping area, auxetic area (area of interest) and unit cell including geometry parameters. All perforations have the same dimensions (**a**, **b**) and distance to its neighbours (**c**) within the entire sheet

rotation of the squares during deformation. The maximum von Mises stress occurs in the thin connecting bars for all specimens, which for specimens from 0 ° to 45 ° gradually decreases with increasing orientation angle. This phenomenon on the macroscale leads to a decline in the global stress, which is responsible for the deformation of the entire sheet. This decrease in global stresses can also be observed in the corresponding global stress–strain curves for the specimens with 0° to 45° rotated pattern (see Fig. 7a). The Young's moduli and yield strengths decrease contineuously with increasing orientation angle.

For the specimens from 45° to 90° rotated pattern, the mechanical properties repeat in such a way that the stress–strain curves related to the specimen with $\theta$ ° rotated pattern are quite identical to the specimen with (90 − $\theta$ )° rotated pattern (see Fig. 7b).

It is obvious that after 90 ° rotation of the pattern, the initial state is recovered, which corresponds to orthotropic materials based on the Table 1. Furthermore referring to the stress-strain curves in Fig. 7, it was also derived that the 45° axis forms an additional axis of symmetry in this structure, which corresponds to the so-called **tetragonal** materials due to the Table 1. A spatial representation of the tetragonal symmetry is shown in Fig. 8, where four of five planes of symmetry lie at distances of 45 ° from each other and the fifth plane of symmetry lies transverse to all of them. The corresponding normal vectors to the planes of symmetry are denoted as $a1 - a5$.

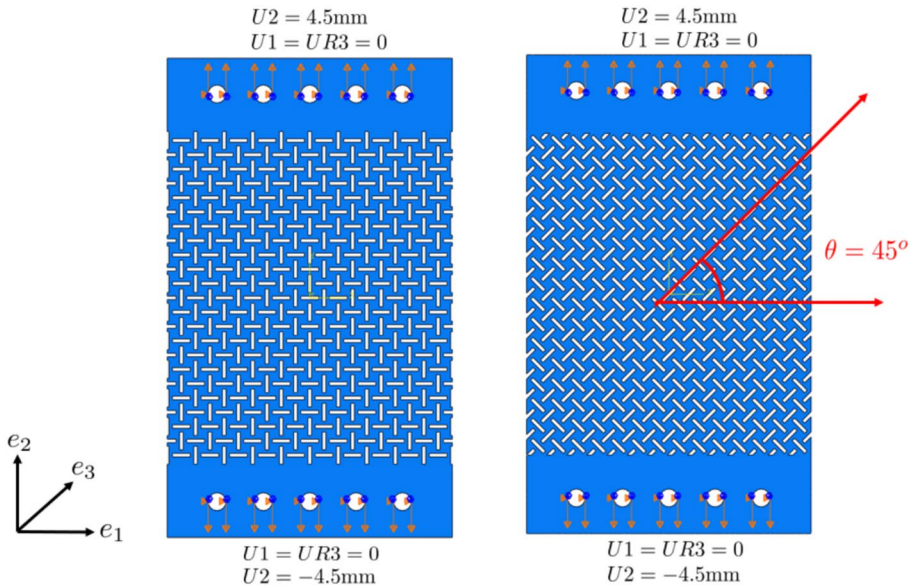


**Fig. 5** the corresponding boundary conditions for the auxetic sheet without pattern orientation (left) and the auxetic sheet with 45 ° pattern orientation angle (right) used to simulate a numerical uniaxial tensile test

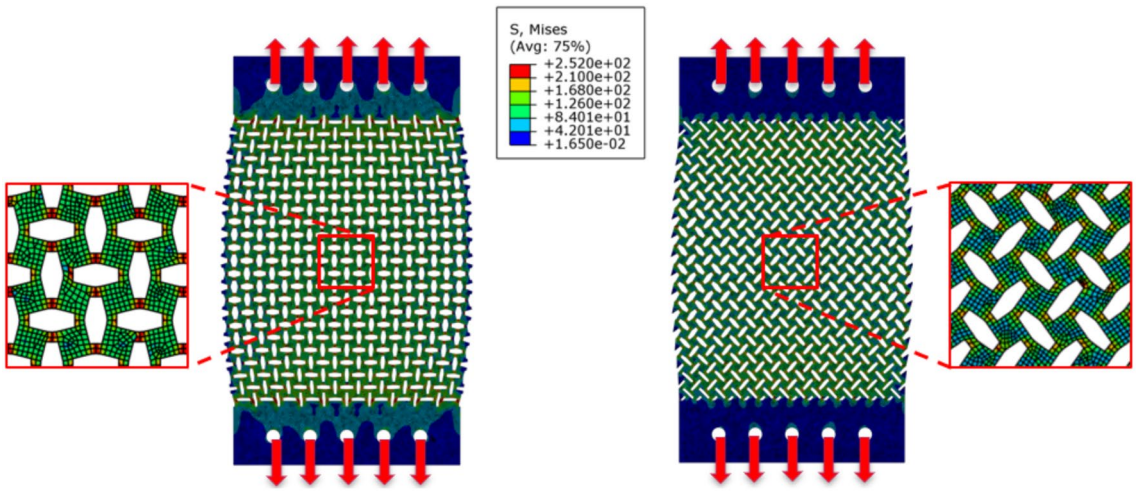


**Fig. 6** The results of numerical simulation of a uniaxial tensile test in terms of local von Mises stress [MPa] on the specimen with 0° pattern orientation (left) and on the specimen with 45° pattern orientation angle (right) after 10% global strain

## 2.2 Numerical homogenization

As discussed in section 1, a suitable RVE for periodic structures as auxetics may consist of one or more unit cells. The exact number of unit cells considered as RVE can be determined by numerical investigations by comparing the global stress–strain curves as well as the existing type of anisotropy of each proposed homogenized RVE with the fully resolved sample. The central point of homogenization is the implementation of Periodic Boundary Conditions (PBCs) to each proposed RVE. Thus, the boundary effects are completely eliminated and the results can be representative for a system consisting of an infinite number of unit cells.

### 2.2.1 Periodic boundary conditions (PBCs)

Periodic Boundary Conditions (PBCs) are actually a set of boundary conditions in form of linear equations between the pairs of nodes, which lying on opposite position on the boundary. In ABAQUS® these equations can either be

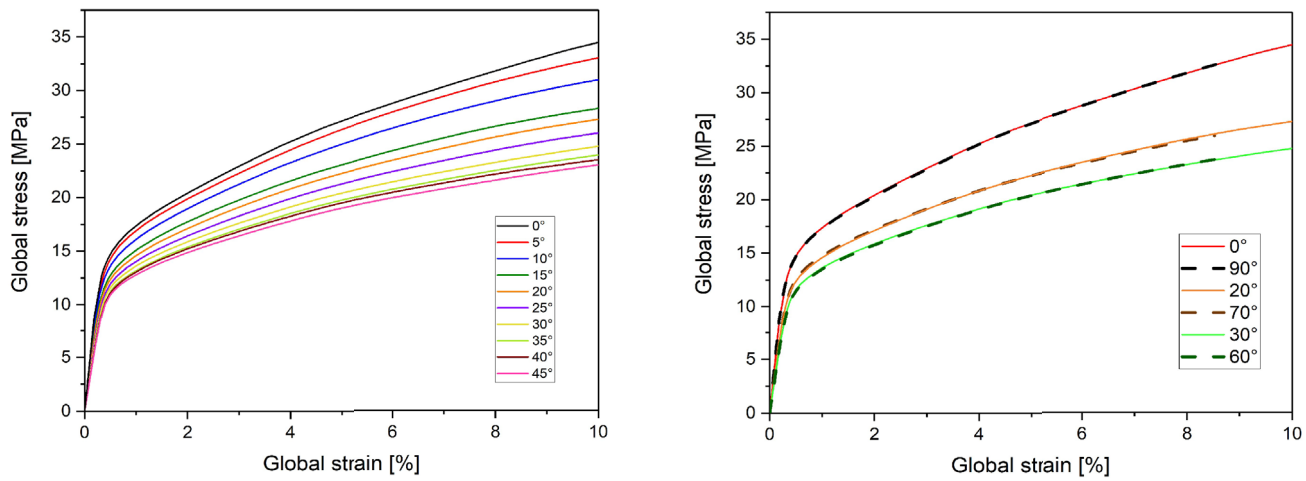


a $0° \leq \theta \leq 45°$ b $0° \leq \theta \leq 90°$

**Fig. 7** Global stress–strain curves related to the specimens with different pattern orientation angles ($\theta$)

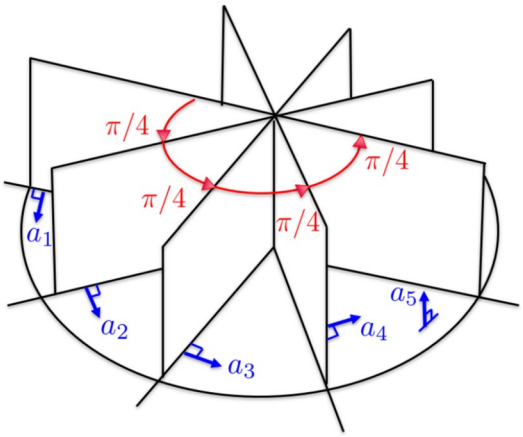


**Fig. 8** Spatial illustration of the five planes of symmetry characterizing tetragonal symmetry. The normals to the five planes are denoted by a1-a5

written directly in the input file or set in ABAQUS-CAE in the interaction module under the constraint-equations. Depending on how the loads and corresponding deformations should look like, these linear equations have to be adjusted. To implement PBCs, all edge nodes must first be selected and stored under the various SETS. The edge nodes, which are opposite to each other, should be easily identified by a meaningful naming as in Fig. 9. In order to automatically identify the opposite pairs of nodes in the rotated samples based on the preferred direction, a coordinate transformation must be performed. Then we need to define a reference point (RP) somewhere outside the model where the desired global displacement of the unit cell is to be applied. To avoid rigid body motion of the whole part, one point on the model must be fixed.

So finally after the above steps we are able to establish the linear equations based on the loading scenario. In general, the equations can be written in four columns, where two columns refer to the node pairs in the loading direction and other two columns refer to the node pairs perpendicular to the loading direction. The necessary number of equations depends on the number of the edge nodes or in other words, it depends on the discretization of the model. The finer the model, the more equations have to be set up. The exact number of equations using the procedure in Fig. 10 is equal to $n + m$, where '$n$' and '$m$' correspond to the total number of the nodes on a horizontal and vertical boundary. For almost all loading scenarios, the form of the equations remains the same and the only thing that needs to be adjusted based on the loading is the displacement vector of the reference point (RP).

For better understanding, we consider two simple load cases, uniaxial tensile load and pure shear load on a single unit cell, which are supposed to be realized by the implementation of PBCs instead of the usual boundary conditions. Figure 10 illustrates the form of the equations as well as the associated displacement vectors based on these loading conditions. As can be seen in the equations, the relative displacement of the East–West node pairs should be a constant value ($l$) and not zero, otherwise, for example, in the uniaxial tensile test, the expansion in transverse direction (auxetic effect) cannot be reproduced. This constant should be formulated as $l_1 = u_1^{rE} - u_1^{rW}$ and $l_2 = u_2^{rE} - u_2^{rW}$, where the node number '$r$' refers to a random node pair exists in East–West direction. The results of the above two loads in terms of the von Mises stress distribution are exhibited in the Fig. 11.

As can be clearly seen in Fig. 11, the edges of the samples with PBC remain straight during deformation and accordingly the stress distribution at the edges is no longer close to zero as in the case of the unit cell without PBCs, but is already under stress, which could represent a unit cell surrounded by many other unit cells in a larger sheet. This is what needs to be considered to determine an appropriate RVE.

#### 2.2.2 Representativ volume element (RVE)

As discussed in section 1, the RVE is in general the smallest volume fraction that represents the properties of the whole system. For periodic systems like auxetics, the RVE consists of one or more unit cells. As demonstrated in Sect. 2.1, the auxetic structure studied in this work exhibits tetragonal symmetry in terms of the anisotropy. This property must also be exhibited by the RVE we are looking for. Moreover, the other mechanical properties such as Poisson's ratio and Young's modulus must be in good agreement as the total system.

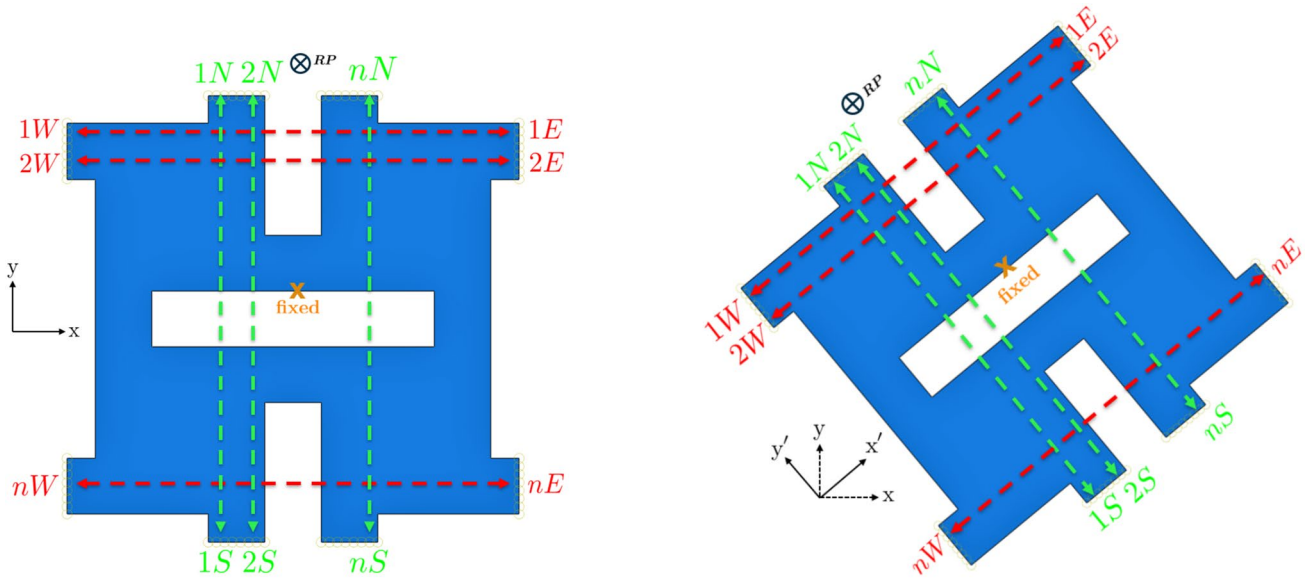


**Fig. 9** Typical way of numbering the node sets at the edges that appear in pairs in the equations when implementing PBCs in case of the standard unit cell (left) and the rotated unit cell (right)

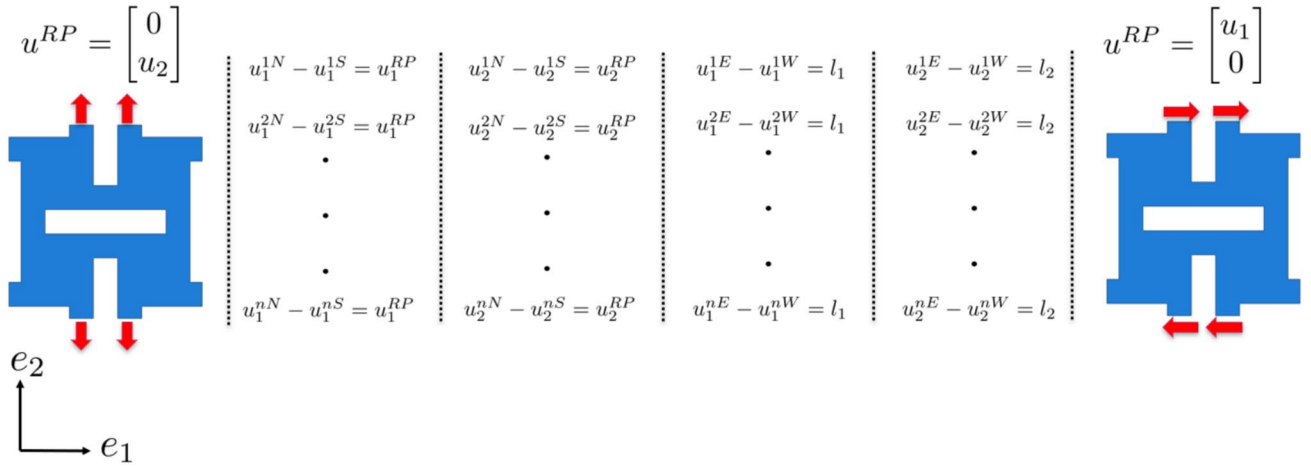


**Fig. 10** Implementation of equations related to the PBCs based on the numbering in Fig. 9 and the displacement vector corresponding to the giving loading condition

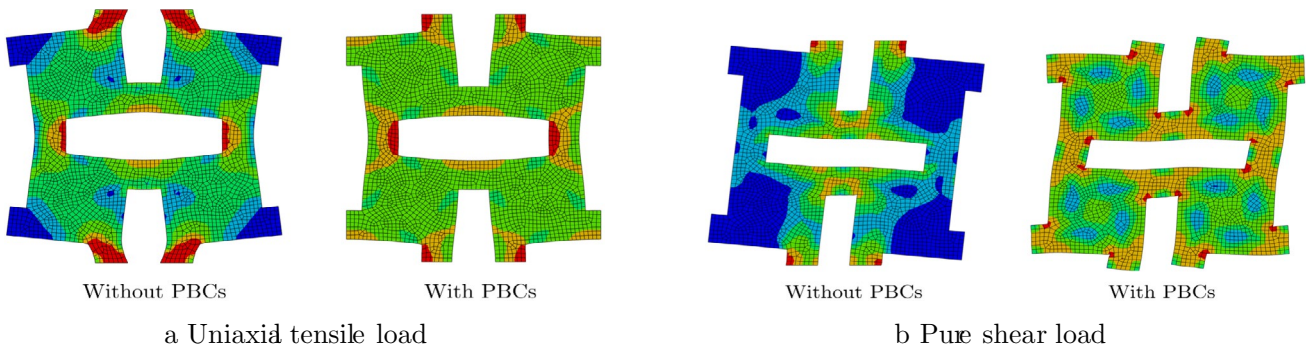


**Fig. 11** The deformed unit cell after the given loads in Fig. 10 respectively with conventional boundary conditions (without PBC) and with Periodic Boundary Conditions (PBCs). The contour represents the local von Mises stress

First a single homogenized unit cell was considered. To investigate the anisotropy, the uniaxial tensile test was also simulated for the homogenized 45° and 90° rotated unit cell. In all three cases, a displacement in $e_2$-direction was specified until 2% global strain is achieved. As can be seen in Fig. 12, the resulting von Mises equivalent stress in the sample with $\theta = 0\,^\circ$ and $\theta = 90\,^\circ$ differ significantly, which as an RVE, may not be the case based on the existing tetragonal symmetry in the overall system. This deviation can also be clearly seen in the global stress–strain curves shown in Fig. 12. According to the resulting displacement fields in the Fig. 12, the $1 \times 1$ unit cell without rotation has a Poisson's ratio of ca. −0.4 in contrast a value of around −0.8 was found for the corresponding fully resolved sample. From these results it can be concluded that the $1 \times 1$ unit cell cannot be a correct RVE for the whole system, because the 1x1 unit cell does not reflect the required symmetry.

As the next step, a homogenized $2 \times 2$ unit cell was considered. In contrast to the $1 \times 1$ unit cell and as can be seen in Fig. 13, the $2 \times 2$ unit cells with $\theta = 0\,^\circ$ and $\theta = 90\,^\circ$ have both quite identical local von Mises equivalent stress and global stress–strain behavior. Both of them also have quite the same Poisson's ratio of about −0.8, which agrees with the Poisson's ratio of the fully resolved sample. It means that the $2 \times 2$ unit cell also approximates a tetragonal symmetry like the fully resolved sample. Moreover, the stress–strain curves of the $2 \times 2$ unit cell and fully resolved sample without orientation ($\theta = 0\,^\circ$) exibit excellent agreement with each other. For the $2 \times 2$ unit cells with $\theta = 45\,^\circ$, the local stresses and displacements look the same as the corresponding fully resolved sample with 45 ° pattern orientation angle. All this information confirms that the $2 \times 2$ unit cells can be chosen as a correct RVE for the whole structure.

After determining the $2 \times 2$ unit cell as a suitable RVE, uniaxial tensile tests were performed on the homogenized RVE with different orientation angles ($\theta$) in 5 ° steps. Accordingly, the corresponding Young's modulus and Poisson's ratio could be determined as the important elastic parameters for each angle. The calculated Young's modulus and Poisson's ratios are represented in Fig. 14 in form of polar diagrams. According to the Fig. 14, there are four symmetry axes on the polar diagrams at intervals of 45° and a fifth symmetry axis transverse to the plane, which corresponds to the tetragonal material symmetry on the basis of Fig. 8.

## 2.3 Anisotropic elasticity

Using the procedure explained in Sect. 1, the corresponding elastic tensor for the auxetic structure studied in this work with tetragonal symmetry can now be determined. It should be noted that in tetragonal materials the orthotropic properties are already included, since $\theta = 0\,^\circ$ and $\theta = 90\,^\circ$ also build symmetry planes in these structures. In other words, tetragonal symmetry can be interpreted as a special case of orthotropy. The difference is that in tetragonal materials there exists an additional symmetry plane at $\theta = 45\,^\circ$, which leads to further restrictions in elastic tensor compared to orthotropic materials. It means we assume the orthotropic elastic tensor as the initial situation and we consider now the transformation (11) using the orthogonal tensor $\mathbf{\Omega}$ in (8) with respect to $\theta = 45\,^\circ$, thus:

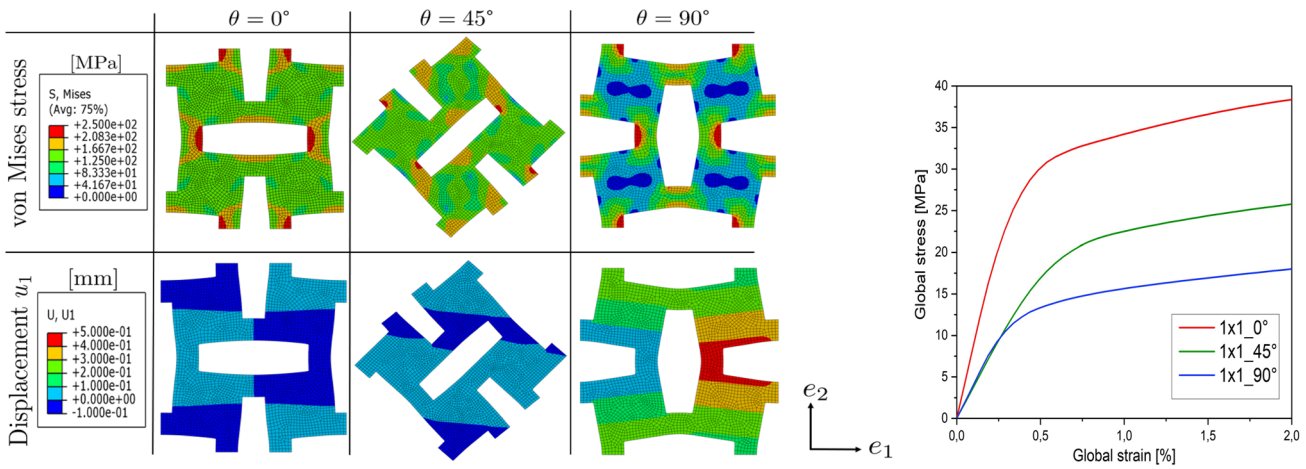


**Fig. 12** Local and global results of uniaxial tensile tests in *y*-direction on the homogenized 1x1 unit cell with different orientation angles until 2% global strain

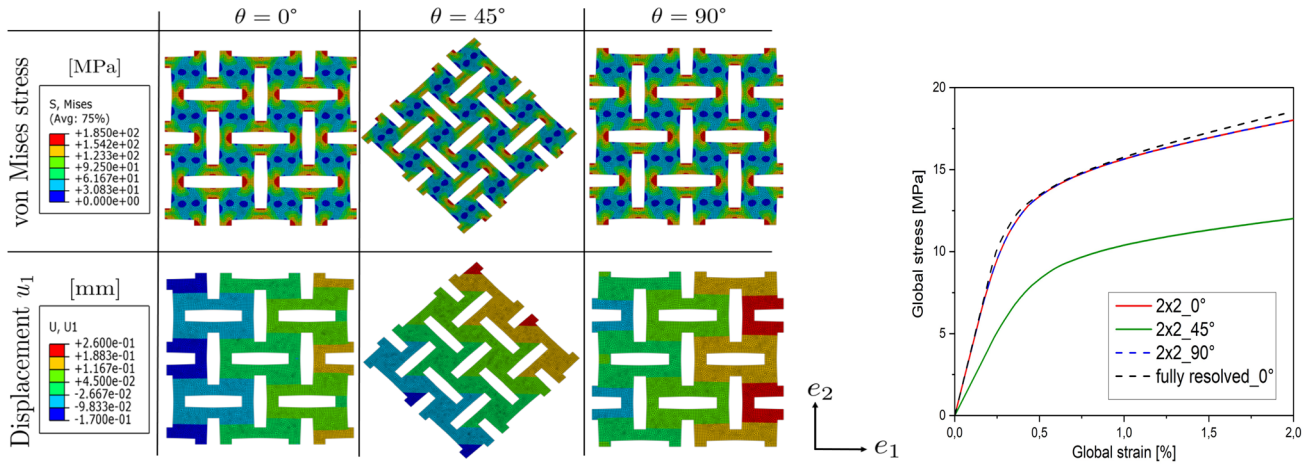


**Fig. 13** Local and global results of uniaxial tensile tests in *y*-direction on the homogenized 2 × 2 unit cell with different orientation angles until 2% global strain

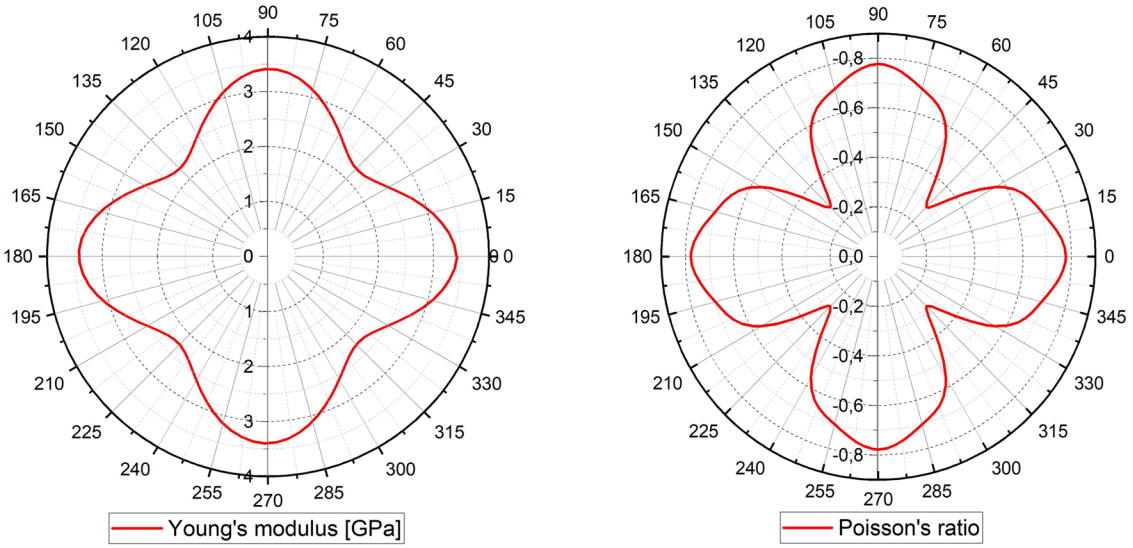


**Fig. 14** Polar diagrams of the homogenized 2 × 2 unit cell as the appropriate RVE of the investigated auxetic structure in terms of Young's modulus and Poisson's ratio

$$\Omega_{ij}(\pi/4) = \begin{bmatrix} 0 & -1 & 0 \\ -1 & 0 & 0 \\ 0 & 0 & 1 \end{bmatrix} \tag{13}$$

The transformation 11 can be written in index notation as follows:

$$C_{ijkl} = \Omega_{ip}\Omega_{jq}\Omega_{kr}\Omega_{lt}C_{pqrt} \tag{14}$$

The zeros in tensor (13) do not contribute to the corresponding summation using the transformation (14). Therefore only the components $\Omega_{12}$, $\Omega_{21}$ and $\Omega_{33}$ have to be taken into account. Due to the symmetry properties of the elasticity tensor $\mathbf{C}$ and also the orthogonal tensor $\mathbf{\Omega}$, the number of components to be considered is reduced to two, i.e. only $\Omega_{12}$ and $\Omega_{33}$, which correspond to either $-1$or $+1$respectively. Now we consider all possible cases in the transformation (14) in which these two components can appear:

$$C_{1111} = \Omega_{12}\Omega_{12}\Omega_{12}\Omega_{12}C_{2222} \longrightarrow C_{1111} = C_{2222} \xrightarrow{\textit{Voigt notation}} C_{11} = C_{22} \tag{15}$$

$$C_{1113} = \Omega_{12}\Omega_{12}\Omega_{12}\Omega_{33}C_{2223} \longrightarrow C_{1113} = -C_{2223} \xrightarrow{\textit{Voigt notation}} C_{15} = -C_{25} \tag{16}$$

$$C_{1133} = \Omega_{12}\Omega_{12}\Omega_{33}\Omega_{33}C_{2233} \longrightarrow C_{1133} = C_{2233} \xrightarrow{\textit{Voigt notation}} C_{13} = C_{23} \tag{17}$$

$$C_{1333} = \Omega_{12}\Omega_{33}\Omega_{33}\Omega_{33}C_{2333} \longrightarrow C_{1333} = -C_{2333} \xrightarrow{\textit{Voigt notation}} C_{53} = -C_{43} \tag{18}$$

$$C_{1313} = \Omega_{12}\Omega_{33}\Omega_{12}\Omega_{33}C_{2323} \longrightarrow C_{1313} = C_{2323} \xrightarrow{\textit{Voigt notation}} C_{44} = C_{55} \tag{19}$$

The transformation results of (16) and (18) do not give any new information since these components are already zero in the orthotropic tensor shown in section (1) and therefore they can be treated as trivial equations. However, the other three results (15), (17) and (19) make the orthotropic tensor even more restrictive in that they must be pairwise equal. Finally the tetragonal compliance tensor $\boldsymbol{S}$ based on the results of (15), (17) and (19) looks like this:

$$\boldsymbol{S}_{Ort} \hat{=} \begin{bmatrix} \frac{1}{E_1} & \frac{-\nu_{21}}{E_2} & \frac{-\nu_{31}}{E_3} & 0 & 0 & 0 \\ \frac{-\nu_{21}}{E_2} & \frac{1}{E_2} & \frac{-\nu_{32}}{E_3} & 0 & 0 & 0 \\ \frac{-\nu_{31}}{E_3} & \frac{-\nu_{32}}{E_3} & \frac{1}{E_3} & 0 & 0 & 0 \\ 0 & 0 & 0 & \frac{1}{G_{13}} & 0 & 0 \\ 0 & 0 & 0 & 0 & \frac{1}{G_{23}} & 0 \\ 0 & 0 & 0 & 0 & 0 & \frac{1}{G_{12}} \end{bmatrix}$$

$$\boldsymbol{S}_{Tet} \hat{=} \begin{bmatrix} \frac{1}{E_1} & \frac{-\nu_{21}}{E_1} & \frac{-\nu_{31}}{E_3} & 0 & 0 & 0 \\ \frac{-\nu_{21}}{E_2} & \frac{1}{E_1} & \frac{-\nu_{31}}{E_3} & 0 & 0 & 0 \\ \frac{-\nu_{31}}{E_3} & \frac{-\nu_{31}}{E_3} & \frac{1}{E_3} & 0 & 0 & 0 \\ 0 & 0 & 0 & \frac{1}{G_{13}} & 0 & 0 \\ 0 & 0 & 0 & 0 & \frac{1}{G_{13}} & 0 \\ 0 & 0 & 0 & 0 & 0 & \frac{1}{G_{12}} \end{bmatrix}$$

Based on the results, the number of independent elastic constants that appear in the compliance tensor $\boldsymbol{S}$ is reduced from 9 (orthotropic) to 6 (tetragonal).

## 3 Implementation and experimental validation

As demonstrated in section 2.3, the corresponding compliance matrix of tetragonal materials has 6 independent elastic constants, namely $E_1$, $E_3$, $G_{12}$, $G_{13}$, $\nu_{12}$ and $\nu_{13}$, which are to be determined experimentally. In a plane stress state, which is the case with the studied auxetic sheet, the number of necessary elastic constants is reduced to 3, namely $E_1$, $G_{12}$ and $\nu_{12}$. In order to determine $E_1$ and $\nu_{12}$, quasi static uniaxial tensile tests were performed experimentally. To calculate the Poisson's ratio, the local displacement fields were observed by the Digital Image Correlation system (DIC). The commercial DIC software ISTRA4D V4.4 by Dantec Dynamics (Skovlunde, Denmark) was employed for post-processing and visualization of the displacements during the deformation. For the computation of homogenized results, the displacements of a $2 \times 2$ unit cell in the center of the sheet in both directions were considered, where the edge effects have minimal influence. The global stress–strain curve and DIC evaluations are presented in Fig. 15, resulting in a Young's modulus and a Poisson's ratio of 1.9 GPa and −0.76, respectively.

The shear modulus $G_{12}$ was also obtained by a corresponding shear test simulation on the homogenized RVE represented in Fig. 16, which results 980 MPa.

After determining the elastic parameters, the developed model was implemented in ABAQUS® as the FE software used in this study. ABAQUS® provides some anisotropic elastic models, which are already implemented in the program, such as for orthotropic material. As discussed in section 2.3, tetragonal symmetry is a special case of orthotropy. Therefore, the implemented model for orthotropic materials can be applied to our auxetic structures. The model for the 2D case can be found in ABAQUS®-CAE under the name "Lamina". Despite the plane stress state defined in Lamina's model, the parameters $G_{13}$ and $G_{23}$ must also be entered in the case of out-of-plane deformations. Due to the present tetragonal symmetry, these two parameters should actually be the same, which was determined by an additional shear test simulation on the RVE in corresponding direction. Finally all input parameters are listed in Table 2, which are used to model the elastic behavior of the auxetic structure.

There is also a possibility to model auxetic sheets with different pattern orientation angles by entering the local coordinate system in material through the module "Property" under the "Assign Material Orientation". The model results are illustrated in Fig. 17 as well as the results of corresponding experiments subjected to uniaxial tensile test on sheets with 0 °, 15 °, 30 ° and 45 ° orientation angle. In all cases, a global strain of 0.5% in $e_2$-direction is specified, which is definitely still within the elastic range of the material. The contours correspond also to the resulting transverse displacements in $e_1$ direction. As can be seen in Fig. 17, the model results reproduced the experimental results quite well with respect to the displacement distributions showing a local deviation of less than 1%.

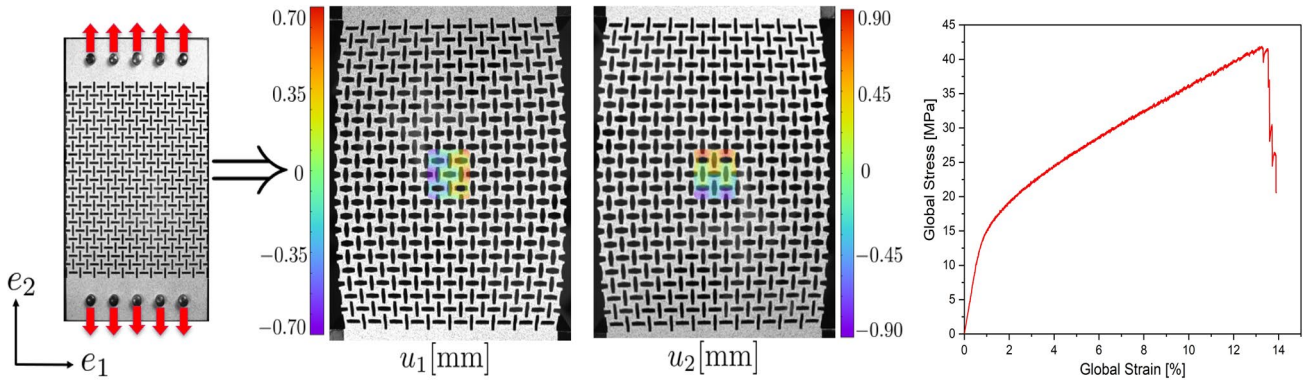


**Fig. 15** Local displacement fields of the 2 × 2 unit cell in the center of the auxetic sheet after about 5% global strain evaluated by DIC and corresponding global stress–strain curve of the sheet caused by uniaxial tensile test

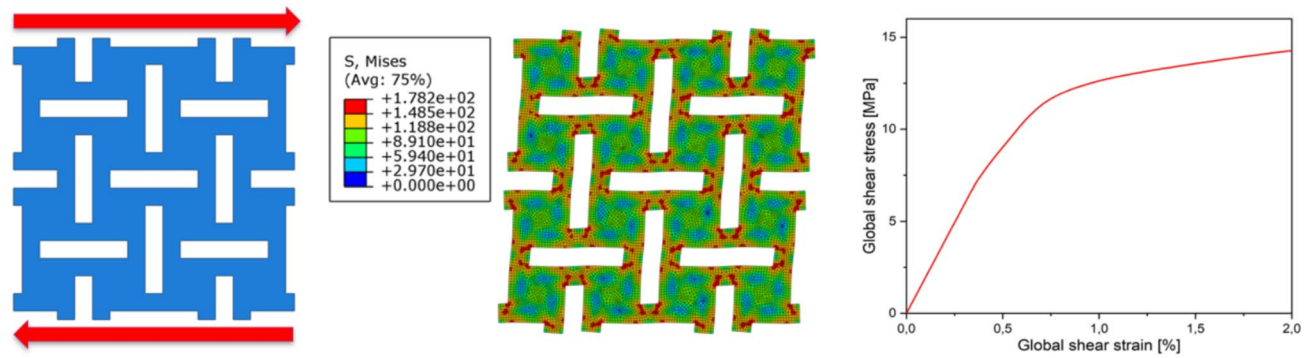


**Fig. 16** Shear test simulation on the homogenized 2 × 2 unit cell as RVE to obtain the shear modulus of the structure

**Table 2** Elastic parameters of the auxetic structure as the input parameters of the applied Lamina's model

| $E_1$ | $E_2$ | $\nu_{12}$ | $G_{12}$ | $G_{13}$ | $G_{23}$ |
|---|---|---|---|---|---|
| 1.9 GPa | 1.9 GPa | −0.76 | 0.98 GPa | 1.3 GPa | 1.3 GPa |

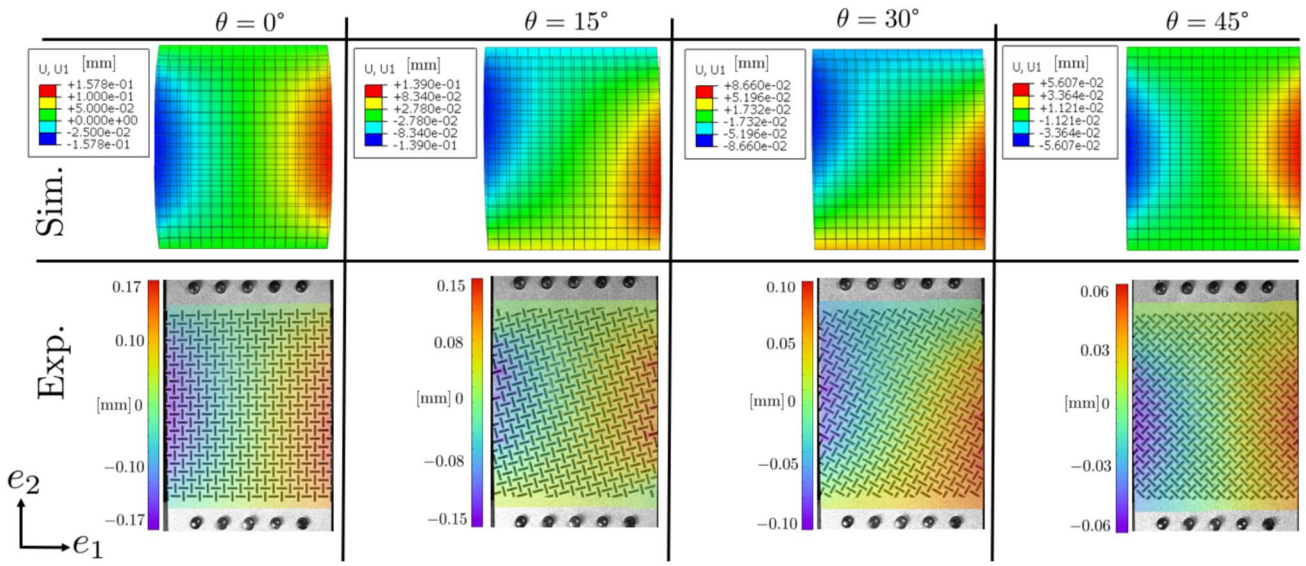


**Fig. 17** Comparison of the resulting transverse displacement fields in $e_1$-direction caused by uniaxial tensile tests in $e_2$-direction after 0.5% global strain imposed by the developed elastic model (simulations) and corresponding experiments

## 4 Conclusion and future work

Auxetic structures are recently developed man-made metamaterials, which due to their exceptional features could have a great bandwidth of applications. A successful deployment of these structures requires detailed and precise research in many areas. In this work, the mechanical behavior of the so-called rotating units auxetic sheet metal was mainly investigated. In this regard an anisotropic tetragonal elastic material model has been developed, which can reproduce the elastic behavior of the structure quite well. Moreover, a convenient Representative Volume Element (RVE) was determined by a numerical homogenization procedure, which represents the effective mechanical properties of these structures as an infinite system. These attainments can be considered and employed as the basic knowledge of these 2D auxetic structures in terms of their mechanical behavior. Obviously, to ensure reliable implementation of these components, further progress would be necessary such as extension of the model to plasticity and even fracture. Furthermore, the development of an anisotropic plastic model for the auxetic sheet would lead also to gain valuable information regarding the behavior of the sheet under different forming processes in which the extended 2.5D or 3D cases such as curved auxetic shell structures and tubes can be manufactured respectively. Therefore, future work will focus on extending the developed elastic model to elasto-plasticity, which is to be experimentally validated under different multi-axial loading conditions.

**Acknowledgements** The authors gratefully acknowledge the funding by Deutsche Forschungsgemeinschaft (Grant No. HE7079/6-1, DI430/32-1).

**Author contributions** Arash Gordanshekan wrote the main manuscript text and wolfgang Ripplinger and Stefan Diebels read the manuscript and gave their comments on it, which have been already considerd in final version of the manuscript.

**Funding** Open Access funding enabled and organized by Projekt DEAL.

**Data availability** The data presented in this study can be obtained on request from the corresponding author.

## Declarations

**Competing interests** The authors declare no Competing interests.

## References

1. Ciallella Alessandro, et al. Deformation patterns in a second-gradient lattice annular plate composed of "spira mirabilis" fibers. Contin Mech Thermodyn. 2023;35(4):1561–80.
2. Cai Jun, et al. Lessons from nature for carbon-based nanoarchitected metamaterials. Small Sci. 2022;2(12):2200039.
3. Aydin Gokhan, et al. Investigating infill density and pattern effects in additive manufacturing by characterizing metamaterials along the strain-gradient theory. Math Mech Solids. 2022;27(10):2002–16.
4. Afshar Reza, Jeanne Simon, Abali Bilen Emek. Nonlinear material modeling for mechanical characterization of 3-D printed pla polymer with different infill densities. Appl Compos Mater. 2023;30(3):987–1001.
5. Casalotti Arnaldo, D'annibale Francesco, Rosi Giuseppe. Multi-scale design of an architected composite structure with optimized graded properties. Compos Struct. 2020;252: 112608.
6. Lakes Roderic. Foam structures with a negative Poisson's ratio. Science. 1987;235:1038–41.
7. Evans Ken E. Auxetic polymers: a new range of materials. Endeavour. 1991;15(4):170–4.
8. Evans Kenneth E, Alderson Andrew. Auxetic materials: functional materials and structures from lateral thinking! Adv Mater. 2000;12(9):617–28.
9. Jae-Hwang Lee, Singer Jonathan P, Thomas Edwin L. Micro-/nanostructured mechanical metamaterials. Adv Mater. 2012;24(36):4782–810.
10. Horst E Friedrich. Leichtbau in der Fahrzeugtechnik. New york: Springer-Verlag; 2017.
11. Grima Joseph N, Ruben Gatt. Perforated sheets exhibiting negative Poisson's ratios. Adv Eng Mater. 2010;12(6):460–4.
12. Wenwang Wu, et al. Mechanical design and multifunctional applications of chiral mechanical metamaterials: a review. Mater Des. 2019;180: 107950.
13. Francisco MB, et al. A review on the energy absorption response and structural applications of auxetic structures". Mech Adv Mater Struct. 2022;29(27):5823–42.
14. Tahir D, Zhang M, Hong H. Auxetic materials for personal protection: a review. Phys Status Sol (b). 2022;259(12).
15. Chetcuti Elaine, et al. Modeling auxetic foams through semi-rigid rotating triangles. Phys Status sol (b). 2014;251(2):297–306.
16. Choi JB, Lakes RS. Non-linear properties of polymer cellular materials with a negative Poisson's ratio. J Mater Sci. 1992;27(17):4678–84.
17. Joseph N, Grima and Kenneth E Evans. Auxetic behavior from rotating squares. Mater Sci Lett. 2000;19:1563–5.
18. Scarpa F, et al. Elastic buckling of hexagonal chiral cell honeycombs. Compos Part A Appl Sci Manuf. 2007;38(2):280–9.
19. Elipe Juan Carlos Álvarez, Lantada Andrés Dıéaz. Comparative study of auxetic geometries by means of computer-aided design and engineering. Smart Mater Struct. 2012;21(10): 105004.
20. Gordanshekan A, et al. Experimental and theoretical investigations of auxetic sheet metal. In: Gordanshekan A, editor., et al., Theoretical analyses, computations, and experiments of multiscale materials: a tribute to Francesco dell'Isola. Berlin: Springer; 2022. p. 689–707.
21. Nemat-Nasser Siavouche, Hori Muneo. Micromechanics: overall properties of heterogeneous materials. Amsterdam: Elsevier; 2013.
22. Hill Rodney. Elastic properties of reinforced solids: some theoretical principles. J Mech Phys Sol. 1963;11(5):357–72.
23. Nguyen VP, et al. On the existence of representative volumes for softening quasi-brittle materials-a failure zone averaging scheme. Comput methods appl mech eng. 2010;199(45–48):3028–38.
24. Gitman IM, Askes Harm, Sluys LJ. Representative volume: existence and size determination. Eng Fract Mech. 2007;74(16):2518–34.
25. Kanit Toufik, et al. Determination of the size of the representative volume element for random composites: statistical and numerical approach". Int J Sol Struct. 2003;40(13–14):3647–79.
26. Abali BE, Yang H, Papadopoulos P. A computational approach for determination of parameters in generalized mechanics. In: Higher gradient materials and related generalized continua. 2019;120, p. 1–18.
27. Spagnuolo M, Franciosi P, Dell'Isola F. A Green operator-based elastic modeling for two-phase pantographic-inspired bi-continuous materials. Int J Sol Struct. 2020;188:282–308.
28. Mizzi Luke, et al. Implementation of periodic boundary conditions for loading of mechanical metamaterials and other complex geometric microstructures using finite element analysis. Eng Comput. 2021;37:1765–79.
29. Xia Zihui, Zhang Yunfa, Ellyin Fernand. A unified periodical boundary conditions for representative volume elements of composites and applications. Int J Sol Struct. 2003;40(8):1907–21.
30. Lijun GAO, et al. Theoretical aspects of selecting repeated unit cell model in micromechanical analysis using displacement-based finite element method. Chin J Aeronaut. 2017;30(4):1417–26.
31. Weidong Wu et al. "Applying periodic boundary conditions in finite element analysis". In: SIMULIA community conference, Providence. (2014), pp. 707–719.
32. Carta Giorgio, Brun Michele, Baldi Antonio. Design of a porous material with isotropic negative Poisson's ratio. Mech Mater. 2016;97:67–75.
33. Cowin SC, Mehrabadi MM. Anisotropic symmetries of linear elasticity. Appl Mech Rev. 1995;48(5):247–85.
34. Cazzani Antonio, Rovati Marco. Extrema of Young's modulus for elastic solids with tetragonal symmetry. Int J Sol Struct. 2005;42(18–19):5057–96.
35. Ting TC, Ting TC. Anisotropic elasticity: theory and applications. Oxford: Oxford University Press on Demand; 1996.
36. Hess Siegfried. Tensors for physics. Berlin: Springer; 2015.